GeoFlowNet-SAR: Earthquake Displacement Estimation from Synthetic Aperture Radar Images

Junjie Wang, James Hollingsworth, Erwan Pathier, Tristan Montagnon, Wei Li, *Senior Member, IEEE*, Mengmeng Zhang, Ran Tao, *Senior Member, IEEE*, Jocelyn Chanussot, *Fellow, IEEE*, Sophie Giffard-Roisin

***Abstract*—Displacement estimation using remote sensing images is an effective approach for assessing surface displacement caused by natural disasters like earthquakes and landslides. By employing pixel correlation algorithms, high-precision displacement maps can be generated from images taken before and after surface movement. However, traditional methods often rely on spatial regularization or frequency masking to reduce high-frequency noise, which can smooth spatial details and result in biased displacement estimates, especially near sharp discontinuities typical of earthquake surface ruptures. Moreover, sub-pixel displacement estimation using Synthetic Aperture Radar (SAR) images remains a challenge compared to optical images, due to the strong impact of speckle noise.**

This paper presents GeoFlowNet-SAR, an innovative sub-pixel displacement estimation method leveraging SAR images. SAR offers advantages thanks to an all-weather observation and high penetration, making it suitable for conditions typically challenging for optical systems in the visible light spectrum. This study uses Sentinel-1 SAR Single Look Complex (SLC) images with dual-polarization (VV and VH modes) and Interferometric Wide (IW) swath mode to balance coverage and resolution. By training on simulated displacement datasets with realistic sharp discontinuities, GeoFlowNet-SAR directly predicts surface displacement fields, providing highly efficient, robust, and precise results, while overcoming some limitations of traditional methods.

The effectiveness of the proposed methodological contribution is first quantitatively demonstrated using synthetic simulated earthquake datasets, including comparisons with state-of-the-art correlation methods. The method is further validated using two real remote sensing images from the 2019 Ridgecrest earthquake and from the 2023 Turkey-Syria earthquake. The observed results from these real datasets confirm the effectiveness of GeoFlowNet-SAR in practical applications. The codes are available at: https://gricad-gitlab.univ-grenoble-alpes.fr/giffards/geoflownet-sar.

***Index Terms*—remote sensing images, displacement estimation, deep learning, synthetic aperture radar.**

I. Introduction

ACCURATE estimation of ground displacement provides critical information for the study of natural hazards related to ground motion (e.g., earthquakes, volcanoes, landslides, etc.) [1]–[4]. When it comes to earthquakes, accurately estimating ground displacement, particularly near-field surface deformation around surface ruptures, provides valuable constraints on the exact location of the earthquake source, the spatial extent of surface damage caused by the earthquake, and potential impact on nearby infrastructure and populations. At the same time, these observational data are crucial for various fields of earthquake science and earthquake engineering.

Recent observational data indicate that the extent of surface slip localization can vary along a fault surface rupture produced during an earthquake [5]–[7]. Although some predictive control parameters have been proposed, the complexity of real-world scenarios means that the mechanisms behind slip variations in surface-rupturing earthquakes are not yet fully understood [8]–[10]. One of the main reasons for this issue is the limited availability of observational data, which makes it challenging to conduct a comprehensive analysis and statistical evaluation of different parameters.

Given this problem, methods relying on image correlation for obtaining displacement maps have been applied and studied [11]–[14]. Image correlation is an image processing technique that estimates the displacement field by calculating the maximum of correlation between two remote sensing images acquired at different times over the same location. This technique is widely used in the study of various surface movements, such as glacier movements, landslides, volcanic eruptions, and surface-rupturing earthquakes [15]–[18]. In the context of earthquakes, the displacements in remote sensing images are typically small compared to the pixel size, necessitating sub-pixel level surface displacement estimation. This is particularly challenging near the surface rupture, where deformation tends to be more complex and sharp, including discontinuities and distributed off-fault deformation.

In recent decades, various methods for quantifying ground deformation from remotely sensed optical images have been extensively studied, and can be broadly classified into two categories: spatial domain-based [19]–[22] and frequency domain-based image correlation techniques [1], [23], [24]. Spatial correlation methods estimate ground displacement by spatially comparing the correlation of a reference image with a second image sampled at different positions within a larger search space (i.e. template matching) [25]. Frequency-based correlation methods perform a similar operation, albeit in the frequency domain, which negates the need for a convolutional-

This paper is supported by the National Key R&D Program of China (Grant No. 2021YFB3900502) and NSFC Projects of International Cooperation and Exchanges (Grant No. W2411055). All of the computations presented in this paper were performed using GRICAD infrastructure (gricad.univ-grenoble-alpes.fr), which is supported by Grenoble (France) research communities. (Corresponding authors: Sophie Giffard-Roisin and Wei Li, sophie.giffard@univ-grenoble-alpes.fr and liwei089@ieee.org)

J. Wang, W. Li, M. Zhang, and R. Tao are with the School of Information and Electronics, Beijing Institute of Technology, Beijing, 100081, China and with the National Key Laboratory of Science and Technology on Space-Born Intelligent Information Processing, 100081, China.

S. Giffard-Roisin, J. Hollingsworth, T. Montagnon, and E. Pathier are with Univ. Grenoble Alpes, Univ. Savoie Mont Blanc, CNRS, IRD, Univ. Gustave Eiffel, ISTerre, 38000 Grenoble, France..

J. Chanussot is with the LJK, CNRS, INRIA, Grenoble INP, University of Grenoble Alpes, 38000 Grenoble, France, and with the Aerospace Information Research Institute, Chinese Academy of Sciences, Beijing 100094, China.

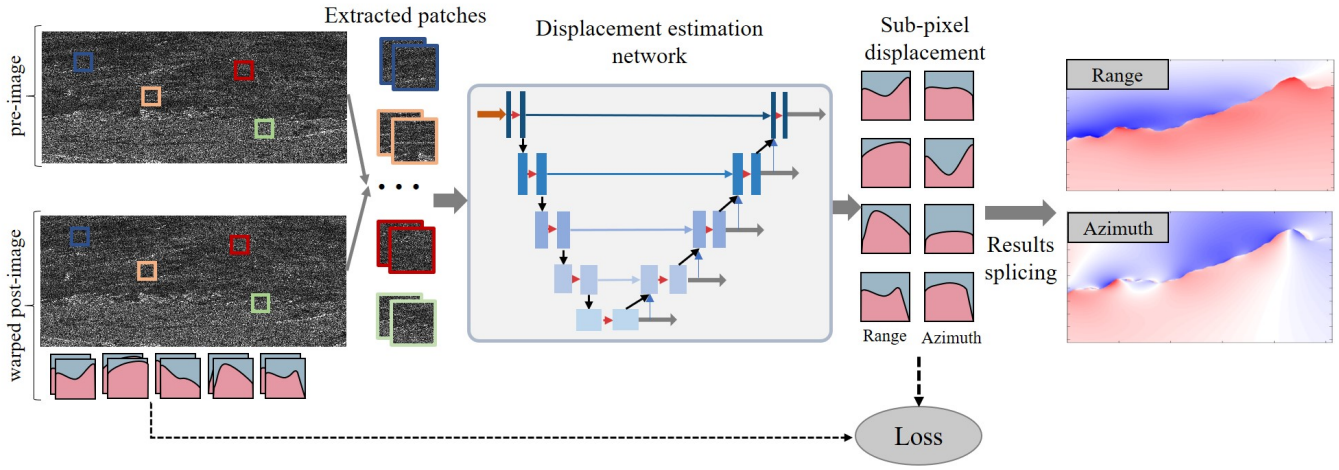

Fig. 1. The flowchart of GeoFlowNet-SAR for sub-pixel ground displacement estimation using SAR images. A pair of input images (pre- and post-event) are acquired on two different dates. Image patches are extracted and fed into GeoFlowNet-SAR, where the model performs sub-pixel displacement estimation, in both range and azimuth directions. The sub-pixel estimation model is trained using synthetic data that includes discontinuities.

type operation, thus making it more efficient [26]. Both methods calculate the local displacement within a sliding window to generate the final displacement field across the whole image. Among them, the Semi-Global Matching (SGM) algorithm [12] approximates the two-dimensional smoothness constraint as the average of one-dimensional line optimization problems, thereby simplifying the computation process. However, this simplification results in characteristic stripe shading in the final output [27]. Furthermore, the SGM approach do not typically achieve high sub-pixel accuracy compared with traditional block-matching approaches. Frequency domain-based methods typically utilize the Fast Fourier Transform (FFT) to compute the upsampled cross-correlation between pre-event and post-event images, and then locate the peak of the correlation [13]. However, as the estimation accuracy increases, the computational burden associated with these methods also rises, particularly in terms of memory requirements.

Meanwhile, although the aforementioned methods have achieved progress in optical image applications, the varying illumination conditions during each acquisition of optical images may affect the content of each pixel, which in turn impacts the correlation process. Additionally, the vegetation and anthropogenic changes between the two acquisitions, separated typically by days to months, makes the estimation process more challenging. Lastly, time between optical satellite acquisitions can become large if cloud coverage prevents the usage of some revisit dates, thereby increasing the differences between the two acquisitions (typically weeks to months or years). In contrast, SAR employs active microwave imaging, which does not rely on external light sources, allowing it to operate effectively also under night conditions. Moreover, the longer wavelength of SAR enables penetration through clouds (as well as some vegetation), facilitating timely, accurate, and spatially detailed imaging of the Earth's surface. However, SAR imaging faces unique challenges that are not present in optical imaging. They are inherently complex due to radar geometric effects such as foreshortening, shadowing, and layover, where taller structures appear disproportionately elongated due to the oblique angle of the radar signal transmission. Additionally, the coherence of radar signals leads to speckle noise, a granular interference that obscures image details and affects the accuracy of analysis. These factors limit traditional optical image processing methods from being directly applied to SAR images. Therefore, it is essential to design and develop displacement estimation methods tailored specifically to the characteristics of SAR data.

Specific correlation methods based have been proposed for SAR images. Li et al. [28] developed a cross-correlation stacking method to suppress the noise floor of Normalized Cross-Correlation (NCC), where the peak height and location in the NCC indicate the matching accuracy and the associated displacement. By stacking a sequence of pairwise NCCs and averaging the resulting NCC stack to determine the offset, the method leverages the redundant information present across multiple NCCs, providing enhanced robustness against noise. Pathier et al. [29] combined offsets results from pairs of SAR images acquired with different geometries of acquisition and used a weighted average method taking into account knowledge about earthquake surface rupture location to prevent averaging displacements on both sides of the sharp discontinuity. These methods attempt to mitigate the impact of SAR image noise from different perspectives. Li et al. [28] leverages statistical redundancy across multiple NCC calculations to suppress noise, while the method from [29] aims to reduce the noise by combining different geometries of acquisition with constraints to reduce spatial inconsistencies. However, both methods face challenges in preserving spatial details: the stacking process may blur fine spatial resolution, and excessive smoothing can obscure critical displacement features. This is particularly problematic near sharp discontinuities, such as those of earthquake surface ruptures, leading to significant deviations in the estimation of slip localization.

In recent years, with the continuous development of deep learning, Convolutional Neural Networks (CNNs) have driven their application in diverse fields such as image classification, scene understanding, and displacement estimation [30]–[33]. Recent studies have begun exploring deep learning techniques for sub-pixel displacement estimation [34], [35], with a few

recent works extending these methods to satellite imagery such as GeoFlowNet [36], [37]. However, these approaches primarily target optical images, which rely on reflected sun light to provide direct surface information. In contrast, SAR images capture the intensity and phase information of radar wave reflections from the surface, presenting unique challenges due to their reliance on intensity and phase information and their susceptibility to speckle noise caused by coherent scattering. This fundamental difference severely limits the direct applicability of optical-based methods to SAR data. Besides, the presence of speckle noise significantly complicates sub-pixel displacement estimation, and consequently existing methods developed for optical imagery are insufficient in mitigating the impact of noise on the estimation results. To the best of our knowledge, there is currently no deep learning-based method designed to address the challenges of sub-pixel displacement estimation in SAR images. Existing optical-based learning models fail to generalize due to their reliance on visual features, which are often distorted or obscured by the noise and scattering effects typical in SAR images. To further substantiate this limitation, additional experiments were conducted by applying an optical-trained model (GeoFlowNet-optical) to SAR imagery. The results clearly demonstrate that such methods struggle to maintain accuracy and robustness, highlighting the necessity of a SAR-oriented design.

Based on the above analysis, the first SAR-specific sub-pixel displacement estimation network GeoFlowNet-SAR based on the deep learning model GeoFlowNet [37] has been developed to address the limitations of prior optical-based approaches. Compared to previous SAR correlation methods, it directly learns and utilizes effective abstract features from the data, reducing the need for manually designed features, simplifying the modeling process, and enhancing the capability to capture relevant features. Additionally, due to its data-driven nature, the model effectively mitigates the impact of noise and other factors (such as atmospheric disturbances) during the feature learning process, enhancing its robustness. Finally, by generating synthetic datasets with sharp discontinuities, it better estimates sub-pixel level sharp changes while preserving spatial details. The main contributions of this paper are:

1) The creation of a large-scale synthetic dataset based on SAR images, leveraging the unique observational characteristics of SAR compared to optical images, enabling the model to perform sub-pixel level ground displacement estimation using SAR images.
2) The development of the first data-based sub-pixel SAR image displacement estimation model GeoFlowNet-SAR, which effectively utilizes multi-scale features within the images, achieving pixel-by-pixel displacement estimation while ensuring spatial detail preservation and robustness across different datasets.

II. Related Work

A. Image correlation methods

Image correlation is a displacement estimation method based on dense non-rigid image registration principles [38]. Its goal is to estimate the displacement between corresponding features (represented by pixels) between two image acquisitions. In most remote sensing images, the transformation between the pre-image and post-image primarily involves a horizontal two-dimensional local displacement field with almost no rotation. It is typically assumed that a global rigid registration has been completed before calculating the displacement field (i.e. the two images are co-registered). In this context, image correlation methods can be broadly categorized into two domains:

1) Spatial correlation methods: Measuring the correlation between two images I_1 and I_2 of the same size involves maximizing a similarity score, which reflects the consistency of the content between the two images. For global registration, the cross-correlation function C_{I_1,I_2} of images I_1 and I_2 can be obtained by computing the pixel-wise product for each possible two-dimensional spatial shift (represented by the components $(\Delta x, \Delta y)$ of the translation vector), and integrating over the entire image domain.

$$C_{I_1,I_2}(\Delta x, \Delta y) = \sum_x \sum_y I_1(x+\Delta x, y+\Delta y) \cdot I_2(x,y) \quad (1)$$

The estimation of the 2D displacement between two images can be achieved by finding the pair $(\Delta x, \Delta y)$, denoted as $(\Delta x^*, \Delta y^*)$, that maximizes the correlation score: $(\Delta x^*, \Delta y^*) = argmax_{\Delta x, \Delta y} C_{I_1,I_2}(\Delta x, \Delta y)$. In this formulation, $(\Delta x^*, \Delta y^*)$ represents a single global shift applied uniformly to all pixels in the image. However, this approach assumes a rigid displacement across the entire image, which does not hold true for scenarios involving varying local shifts. In such cases, the result may represent an average of the varying displacements rather than the true dense motion field. While this formulation is appropriate for global registration, it does not capture the spatially varying flows required for dense flow estimation, which is the primary focus of this study. To capture finer local variations, a local spatial segmentation method is employed. This approach divides the image into multiple sliding rectangular windows of a predefined size, where each window $W_{k,l}$ corresponds to a subset of pixels centered at coordinates (k, l). By analyzing smaller regions, this method enables a more detailed estimation of local displacements. For each window $W_{k,l}$, the cross-correlation function is computed as follows:

$$C_{I_1,I_2}(k,l,\Delta x, \Delta y) = \sum_x \sum_y W^1_{k,l}(x+\Delta x, y+\Delta y) \cdot W^2_{k,l}(x,y) \quad (2)$$

Then $(\Delta x^*_{k,l}, \Delta y^*_{k,l})$ (which corresponds to the displacement vector that maximizes the correlation score at position (k, l)) can be calculated from $C_{I_1,I_2}(k,l,\Delta x, \Delta y)$:

$$(\Delta x^*_{k,l}, \Delta y^*_{k,l}) = argmax_{\Delta x, \Delta y} C_{I_1,I_2}(k,l,\Delta x, \Delta y) \quad (3)$$

2) Frequency correlation methods: An alternative method involves using the frequency domain. The fundamental principle is calculating the normalized cross-power spectrum Q_{I_1,I_2}, which is derived by multiplying the Fourier transform $\mathcal{F}(\cdot)$ of one image with the complex conjugate of the Fourier transform of the other image on an element-wise basis. The inverse

Fourier transform $\mathcal{F}^{-1}(\cdot)$ is applied to this product, resulting in a normalized cross-correlation matrix $R_{I_1,I_2}(\Delta x, \Delta y)$:

$$R_{I_1,I_2}(\Delta x, \Delta y) = \mathcal{F}^{-1}\left\{\frac{\mathcal{F}(I_1)\mathcal{F}^*(I_2)}{|\mathcal{F}(I_1)\mathcal{F}(I_2)|}\right\} \quad (4)$$

The relative displacement between the two images is subsequently determined by identifying the positions of the peaks within the correlation matrix [13]. To estimate the displacement field across the entire image, the two images are divided into multiple windows similarly to spatial correlation methods.

Frequency-based correlation methods help reduce the impact of high-frequency noise and maintain reasonable computational costs, but this often comes at the cost of losing spatial detail. Using larger correlation windows can achieve an optimal balance between accuracy, noise control, and spatial detail. However, in areas with sharp discontinuities or complex displacements, frequency-based methods may introduce biases due to the assumption of a homogeneous translation.

B. Deep learning-based methods

Deep learning algorithms, particularly CNNs, have achieved remarkable success in image processing and computer vision tasks due to their powerful feature extraction and hierarchical pattern recognition capabilities. As a core architecture of deep learning, CNNs leverage a combination of convolutional layers, pooling layers, normalization layers, activation functions, and fully connected layers to learn complex features from images and map them to task-specific outputs. Previous works in computer vision have shown that displacement fields between two natural images can be efficiently estimated by deep learning optical flow [39] based on U-Net architectures. Then Montagnon et al. [36] introduced the first CNN-based model for sub-pixel ground displacement estimation for optical satellite imagery. While traditional CNN architectures are effective, they face challenges in capturing both global and local contexts simultaneously — an essential aspect for sub-pixel displacement estimation. To overcome these limitations, Montagnon et al. [37] derived an optical flow U-Net architecture that they called GeoFlowNet (we will call it GeoFlowNet-optical in this paper for more clarity), able to estimate a dense field at a large scale thanks to the first realistic fault displacement database using optical images called FaultDeform. This approach better preserves spatial details and reduces computational redundancy.

However, these methods are focused on satellite optical images, without specifically addressing sub-pixel displacement estimation using SAR images. Therefore, this paper explores the use of a U-Net architecture combined with SAR images to achieve sub-pixel ground displacement estimation. By leveraging the multi-scale feature extraction capability of U-Net and a specifically designed synthetic database called FaultDeform-SAR, a novel displacement estimation method GeoFlowNet-SAR is proposed.

III. Methodology

A. Overview

The process for sub-pixel ground displacement estimation using GeoFlowNet-SAR is illustrated in Fig.2. The input images are two amplitude radar images from different times P_1 (the pre-image) and P_2^w (the warped post-image). Both have dimensions $s \times s$, where s is the size of the sliding window, adjustable as needed (typically 256, 512, or 1024).

The model processes and correlates the input data through a U-net feature pyramid structure to obtain the final predicted displacement map. During the training and validation phases, the input data consists of pairs of images and their corresponding synthetic displacement maps. The generation of this specific synthetic database FaultDeform-SAR will be the purpose of the next sub-section. The GeoFlowNet-SAR network parameters are continuously optimized by computing a multi-scale loss between the predicted displacement map and the ground truth displacement values, enabling the model to achieve satisfactory performance. For the prediction on real data, the displacement estimations from the different sliding windows are stitched together to produce the final result.

B. Generation of the training database FaultDeform-SAR

In real-world scenarios, very precise and spatially dense ground displacement measurements following natural disasters such as earthquakes are usually unavailable, which creates a significant challenge for the training of data-based ground displacement estimation. Moreover, there is currently no publicly available SAR image dataset, real or synthetic, that can be used for ground displacement estimation.

To effectively train the network parameters, a synthetic remote sensing database with predefined displacements was developed for training and validation. Building on a recent database FaultDeform that proposed realistic synthetic earthquake displacement fields warping real optical imagery [37], our new FaultDeform-SAR dataset applies the same subpixel displacement fields to real SAR image patches, enabling subpixel displacement estimation. To help clarify the generation pipeline of the FaultDeform-SAR dataset, the key steps are summarized below:

Step 1: Select stable SAR image pairs P_1 and P_2 acquired over the same location with natural changes but without actual ground deformation.

Step 2: Apply global image alignment using phase correlation to ensure perfect patch-level spatial correspondence.

Step 3: Generate synthetic, non-uniform displacement fields $\&$ that simulate earthquake deformations with sharp discontinuities.

Step 4: Warp the post-event image P_2 using the displacement field $\&$ to obtain the warped image P_2^w.

Step 5: Form the training sample triplet: (P_1, P_2^w, $\&$), as visualized in Fig. 3.

Specifically, the database consists of Sentinel-1 satellite images of the SAR Single Look Complex (SLC) product type, which capture both phase and amplitude. The FaultDeform-SAR focuses only on amplitude information, which uses the VV polarization mode and operates in the Interferometric Wide (IW) swath mode to ensure balanced coverage and resolution. The images were collected in a side-looking geometry during a descending orbit, ensuring comprehensive coverage and consistent illumination. Sentinel-1's use of the C-band frequency (approximately 5.405 GHz) allows for strong

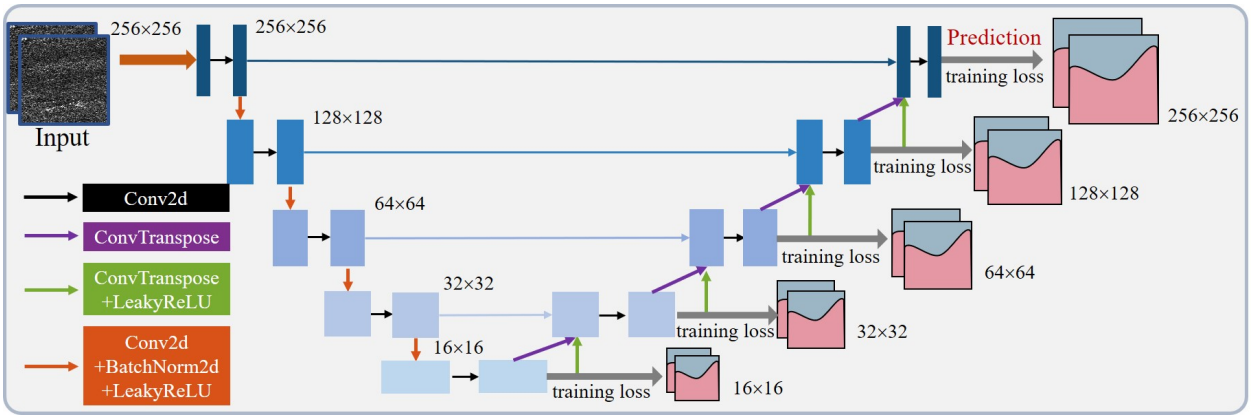

Fig. 2. The architecture of the GeoFlowNet-SAR model for sub-pixel ground displacement estimation. The model takes pre- and post-amplitude radar images as input and outputs the estimated displacement map.

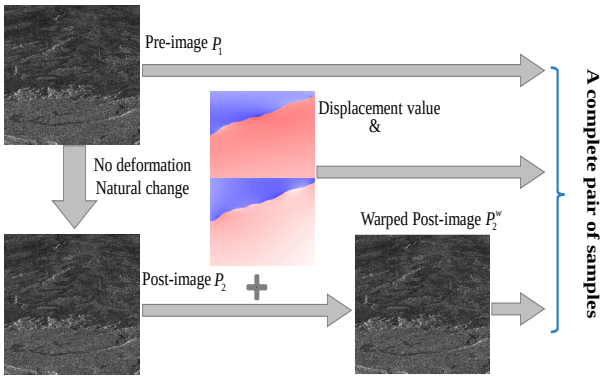

Fig. 3. Generation of a pair of simulated synthetic earthquake images. The warped post-image incorporates natural reflectance differences due to the time gap between the pre- and post-image acquisitions, along with the generated displacement values. The pre-image, warped post-image and displacement map form a complete pair of sample.

penetration through clouds and light vegetation. The spatial resolution of the data is defined by a range pixel size of 2.3 meters (range spacing measured along the radar line of sight) and an azimuth pixel size of 15.6 meters, supporting detailed surface analysis.

In addition to the differences caused by real displacements, image offset measurements in real-world scenarios are also influenced by various reflective noise, such as lighting (for optical sensors) or topographically correlated amplitude variations and vegetation changes. Therefore, Synthetic Aperture Radar (SAR) images covering four distinct locations in the United States with specific time intervals between acquisitions are utilized: California (June 25, 2023, to July 7, 2023), Arizona (August 4, 2023, to August 16, 2023), Colorado (January 12, 2023, to January 24, 2023), and Oregon (March 2, 2023, to March 14, 2023). These SAR images, which contain no ground displacement, serve as pre- and post-event images, allowing us to distinguish between true surface displacement and noise artifacts from environmental factors, thus enhancing the reliability of displacement measurements under varying temporal and environmental conditions. Additionally, phase correlation (implemented in Python using the matrix-multiplication Discrete Fourier Transform (DFT) method) is employed to globally align the two acquired images, reducing potential global mis-registration errors that may remain after the standard pre-processing steps applied to Sentinel-1 images by the European Space Agency (ESA). Following the alignment of the two images from different times, corresponding image patches are extracted from identical locations within the radar amplitude images, ensuring that the two patches (P_1 and P_2) represent the same area captured at different times.

Subsequently, a synthetic displacement field & containing sharp discontinuities was created to warp P_2, generating a warped version P_2^w, that simulates ground displacement. To accurately reflect real-world surface displacements, which often display rough geometries and slip distributions due to natural fault discontinuities, the synthetic displacement field is designed to be non-uniform. The displacement field is derived using analytical expressions that link slip on triangular faults to surface displacements, and is computed from a set of randomly generated (and rough) fault geometries and earthquake slip distributions. Moreover, we specifically design a database with anisotropic deformation magnitudes in order to account for the specificity of SAR acquisitions: the size of the pixel is larger in azimuth than in range. A complete sample in the training dataset consists of a pair of training images (P_1, P_2^w) and the corresponding displacement field &, used as ground truth. This process can be summarized as:

$$\begin{aligned} P_2(x,y) &= e_{\Delta t}(P_1(x,y)), \\ P_2^w &= f_{\&}(P_2(x,y)) \end{aligned} \tag{5}$$

where $e_{\Delta t}$ represents the natural evolution of the ground over the time interval Δt, while $f_{\&}$ denotes the warp operation associated with & (see [37] for more details). To meet the requirements of model training, this process was repeated multiple times (including extracting blocks from large-scale remote sensing images and generating synthetic displacement fields) to create a sufficient number of samples, and the complete workflow is illustrated in Fig. 3. The resulting dataset contains 20,000 samples, each with a size of 1024×1024 pixels, with 90% used for training and 10% for validation, and testing conducted on real data as well as additional generated synthetic data.

C. Sub-pixel estimation model GeoFlowNet-SAR

The model takes two image patches, P_1 and P_2^w from two time phases, as input and produces an output of displacement estimation of the same size as the input. This output consists of two components, representing the subpixel wise displacement values in the row and column directions, corresponding to the azimuth and range directions in the SAR images.

Specifically, the proposed GeoFlowNet-SAR consists of an encoder and a decoder. The image patches from two different time phases, taken from the same location, are passed through an encoder consisting of five convolutional layers. Starting from the second layer, the spatial dimensions are progressively reduced while the channel dimensions are increased. A ReLU activation function follows each convolutional layer. The number of filters gradually increases from 32 to 512, with a uniform kernel size of 3×3, which helps to extract fine-grained features from the small feature maps [40]. Pooling layers are not used in this process to maximize spatial information. Instead, dimensionality reduction is achieved through the use of strided convolutions, which effectively capture multi-scale features. The decoder part consists of corresponding transposed convolution layers that gradually restore the dimensions of the feature maps. These are then concatenated with the previous features, allowing the model to better integrate the scale features captured during the encoding phase, thus effectively handling ground displacement across different scales in large-scale scenarios. The design of the model aims to enhance displacement estimation accuracy across various scales by utilizing windows of different sizes. The specific structure and parameters are detailed in Fig.2. After obtaining displacement predictions across different scales, the difference between the predicted and ground truth displacement values are quantified to compute the loss function. To ensure balanced learning across all scales, a multi-scale loss function is employed to guide the training process [40]. Specifically, the loss function comprises the Mean Absolute Error (MAE) between the predicted displacements and the ground-truth displacements at each scale. These scale-specific losses are then weighted and summed to reflect the importance of features at different scales. This approach enables the network to learn global displacement patterns at coarse scales while also capturing detailed variations at finer scales. This multiscale approach benefits backpropagation by distributing the gradients across scales, reducing the risk of vanishing or exploding gradients associated with single-scale optimization. Eventually, the model generates precise displacement estimations for displacement fields across different scales, providing more accurate decision-making support for subsequent tasks.

IV. Experimental Results and Discussions

A. Implementation details

Experiments are conducted within a Linux operating system using the PyTorch framework. All experiments are performed on an NVIDIA Tesla V100 NVLink GPU. Adam optimization algorithm (Adaptive Moment Estimation) is employed, and multiscale MAE is used as the loss function. The initial learning rate is set to 0.001, and a cosine annealing schedule is used to adjust the learning rate during training. The input image size is standardized to 256×256 pixels, and a batch size of 32 is selected for the experiments.

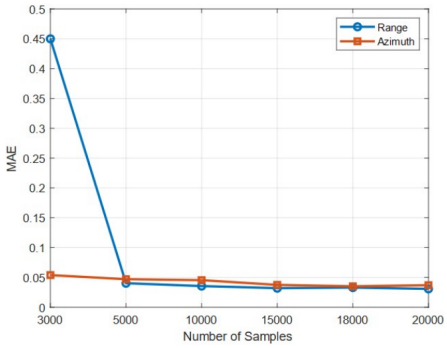

Fig. 4. Mean Absolute Error (MAE) of the validation synthetic set with respect to the number of training samples.

B. Testing on a synthetic earthquake database

For comprehensive evaluation, synthetic data similar to the training set is used for testing, comprising different samples from various areas but generated in the same manner (see Section III-B). These samples are derived from distinct Sentinel-1 satellite patches, collected at different time intervals. Simulated displacement fields are applied to the post-images, and the process involves precise co-registration and spline resampling to introduce realistic surface displacements with subpixel accuracy (approximately $1/100$ of a pixel). This ensures rigorous testing and allows for effective comparison of the proposed model's performance against other methods.

1) Comparisons with state-of-the-art methods: Mean Absolute Error (MAE) is utilized as the metric for quantitative analysis. The performance of different methods was evaluated by comparing the predicted ground displacement estimation against the simulated displacement data used in generating the synthetic earthquake images. COSICorr [41], Ampcor [42], and GeoFlowNet-optical [43] are employed as representative displacement estimation methods and serve as comparative benchmarks.

Specifically, the advanced frequency-based correlator, COSICorr-frequency, estimates ground displacement directly in the frequency domain, thereby avoiding the computational burden of inverse Fourier transforms. Additionally, the spatial correlation-based method, COSICorr-spatial, is also employed to demonstrate its diverse and robust predictive capabilities. Meanwhile, Ampcor, one of the most commonly used feature tracking algorithms (packaged in the ROI_PAC and ISCE SAR processing software), enhances ground displacement tracking between SAR images by applying different kernels (e.g., normalized/unnormalized Wallis filters) for high-pass filtering. Lastly, GeoFlowNet-optical is a U-Net-based deep learning method trained on a realistic synthetic dataset (FaultDeform) to estimate full-field ground displacements from optical imagery. To provide a more intuitive comparison of the estimation results, the predicted outcomes of different methods on the synthetic earthquake images were visualized. (Note that

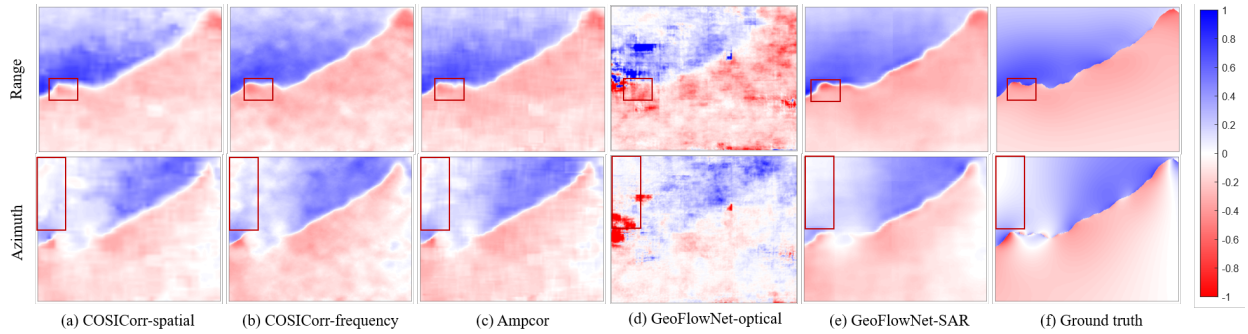

Fig. 5. Displacement maps generated by five models—COSICorr-spatial, COSICorr-frequency, Ampcor, GeoFlowNet-optical, and GeoFlowNet-SAR on a synthetic earthquake sample. The first column shows displacement maps in the range direction, and the second column shows displacement maps in the azimuth direction. The ground truth refers to the synthetic displacement map used to warp the two satellite images. The results are presented in units of pixels.

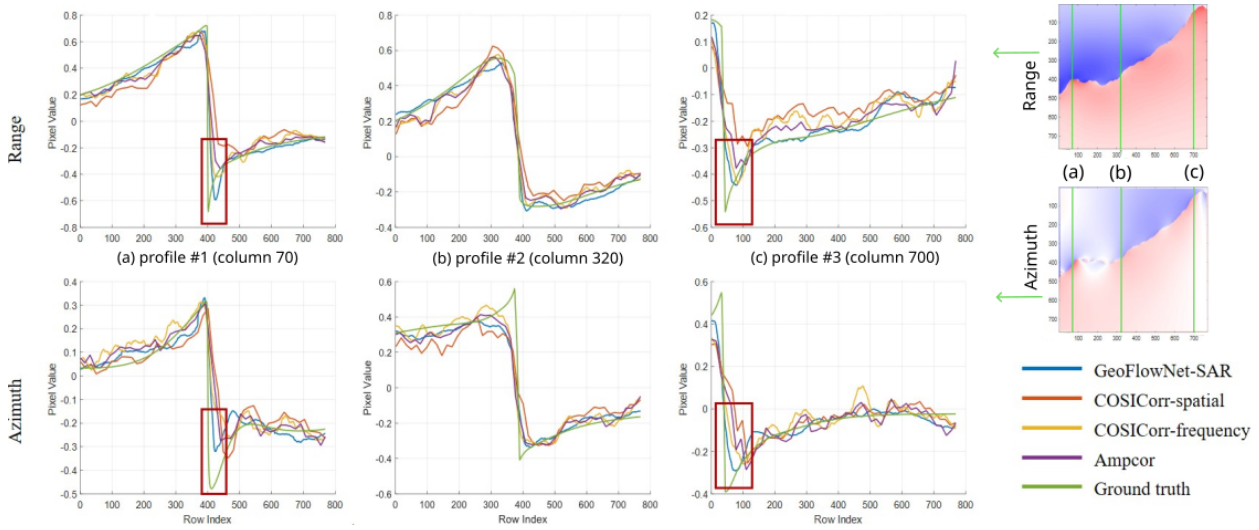

Fig. 6. Curves of 3 profiles of the displacement map from Fig. 5 generated by the five models—COSICorr_spatial, COSICorr_frequency, Ampcor, and GeoFlowNet-SAR. Results are expressed in pixels Top: range, Bottom: azimuth.

in the synthetic earthquake images, all displacement values are kept within the range of [-1,1], as our primary focus is on evaluating the performance of the model at sub-pixel displacement estimation tasks.)

Before conducting the comparison of different methods, the optimal parameter configurations for COSICorr and Ampcor were investigated. The performance of COSICorr-spatial, COSICorr-frequency, and Ampcor was evaluated across various combinations of stride $[1, 2, 4, 8, 16]$ (starting from 2 for COSICorr-frequency) and window sizes $[32, 64, 128, 256]$. The COSICorr-spatial method achieved the best estimation performance with a stride of 16 and a window size of 64, which is selected as the optimal configuration for subsequent experimental comparisons. Similarly, the COSICorr-frequency method achieved the best Range and Azimuth estimation performance with a stride of 2 and a window size of 128. For Ampcor, the lowest MAE was obtained with a stride of 16 and a window size of 64.

For GeoFlowNet-SAR, the number of training samples significantly impacts the effectiveness of model training. To investigate this parameter, the total number of samples was verified to observe its effect on the performance of the model. The total number of samples was set to $[3000, 5000, 10000, 15000, 18000, 20000]$ sequentially, with 90% of the samples used for training. According to the validation results in Fig.4, the model exhibited the best performance when the number of samples is 20,000. However, the improvement in performance compared to using 18,000 samples is relatively marginal. Therefore, considering the balance between training costs and time efficiency, the number of training samples was not further increased. In the subsequent experiments, the comparative results used were derived from models trained with 90% of 18,000 samples.

The proposed method utilizes a sliding 256×256 pixel window in case of a larger input image. Since the prediction output is the same size as the input, the final displacement map is then obtained by averaging the predictions value for each position in overlapping regions (we typically perform 4 predictions for each location). Fig.5 shows the azimuth-directed displacement maps and range-directed displacement maps obtained by different methods on this synthetic earthquake sample. First, we can see that the original GeoFlowNet-optical is not reaching a competitive result. The overall contours obtained by the four other methods are similar. However, there are noticeable differences in texture and fault boundary clarity. The results predicted by GeoFlowNet-SAR exhibit richer texture infor-

mation and higher distinction near fault zones. Additionally, as highlighted in the red-boxed regions, the estimation of boundary areas is more closely aligned with the ground truth. To provide a more detailed comparison of the estimation among different methods, three representative profiles were selected for analysis. Fig.6 highlights that GeoFlowNet-SAR not only achieves peak predictions at fault boundary areas that are more closely aligned with the ground truth but also exhibits smoother fluctuations across the entire strip region. Despite using the optimal parameter configurations, the comparative methods still produce correlation maps with higher noise levels than those obtained by GeoFlowNet-SAR.

TABLE I
MEAN ABSOLUTE ERROR (MAE) OF DIFFERENT METHODS ON THE SYNTHETIC EARTHQUAKE DATABASE (VALIDATION SET)

Methods \ Directions	Range	Azimuth
COSICorr-spatial	0.0659	0.0776
COSICorr-frequency	0.0498	0.0471
Ampcor	0.0456	0.0425
GeoFlowNet-optical	0.1814	0.1900
GeoFlowNet-SAR	**0.0326**	**0.0378**

Table I lists the Mean Absolute Error (MAE) values calculated across a whole validation displacement map (1024×1024) for the different methods. The global errors range from $3.26e{-}2$ to $7.76e{-}2$ pixels, with higher errors generally observed in the azimuth direction due to its lower spatial resolution. The proposed GeoFlowNet-SAR achieves the lowest errors ($3.26e{-}2$ in the range direction and $3.78e{-}2$ in azimuth), outperforming COSICorr-spatial, COSICorr-frequency, Ampcor,and GeoFlowNet-optical. Visual comparisons in Fig. 5 indicate that both COSICorr methods struggle with spatial details, while GeoFlowNet-SAR provides smoother estimations and better captures sharp changes near fault ruptures. GeoFlowNet-SAR outperforms in both precision and spatial detail preservation.

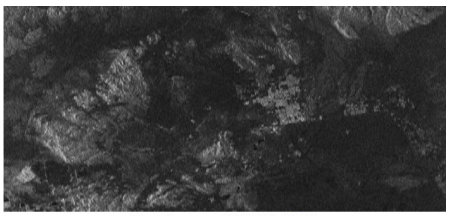

Pre-image(20190622)

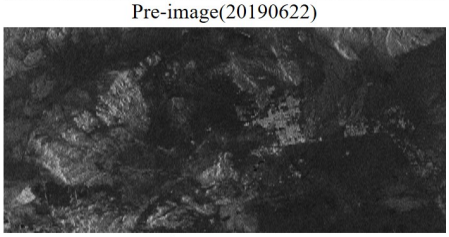

Post-image(20190716)

Fig. 7. The pre- and post- SAR images of Ridgecrest earthquake.

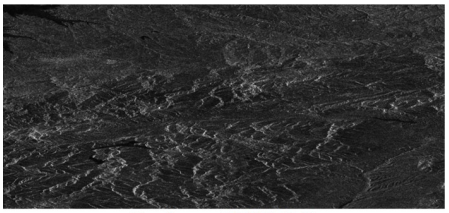

Pre-image(20230129)

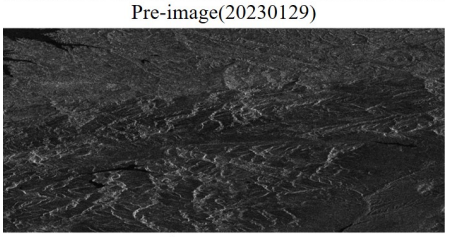

Post-image(20230210)

Fig. 8. The pre- and post- SAR images of Turkey-Syria earthquake.

C. Testing on Real Earthquake Cases

1) Ridgecrest Earthquake: On July 4 and 7, 2019, Ridgecrest in Southern California's Mojave Desert was hit by a significant earthquake sequence, beginning with a foreshock causing a rupture along a northeast-southwest oriented left-lateral fault, followed by a mainshock, triggering a rupture on a conjugate right-lateral fault with a northwest-southeast orientation. For this sequence, various studies utilized remote sensing images spanning the two earthquakes to estimate near-field ground displacements associated with the surface ruptures. The resulting displacement maps allowed for evaluation of the local strain field, thereby providing fresh insights into the fault slip mechanism, and the degree of slip localization and fault zone width along the rupture [9], [22], [43].

Since the images used during the training phase are derived from simulated synthetic data, it remains an open question whether the model adapts well when applied to images from real cases. For this real earthquake scenario, we compare the proposed model with COSICorr-spatial, COSICorr-frequency, Ampcor, and GeoFlowNet-optical. The purpose of this comparison is to evaluate the performance of GeoFlowNet-SAR on remote sensing images containing actual earthquake-induced displacements, beyond just the synthetic earthquake data. This also presents an opportunity to assess the robustness of the model across different scenarios. For the Ridgecrest earthquake, no publicly available ground truth displacement maps currently exist. Nevertheless, comparing the displacement results generated by different methods helps assess the consistency between the proposed model and existing well-established image correlation techniques. Moreover, visual inspection of the displacement field near the fault rupture and the presence of high-frequency noise in the displacement maps partially reveal the errors identified by the different methods.

In addition, displacement estimation results using optical imagery for this earthquake case are introduced as a reference for comparison, where the optical displacement maps were derived from high-resolution optical imagery (SPOT6 for Ridgecrest) using the COSI-Corr-frequency method, which is widely recognized as a standard for image correlation. The reference map was produced with multiscale frequency windows, and further cleaned through expert geological post-

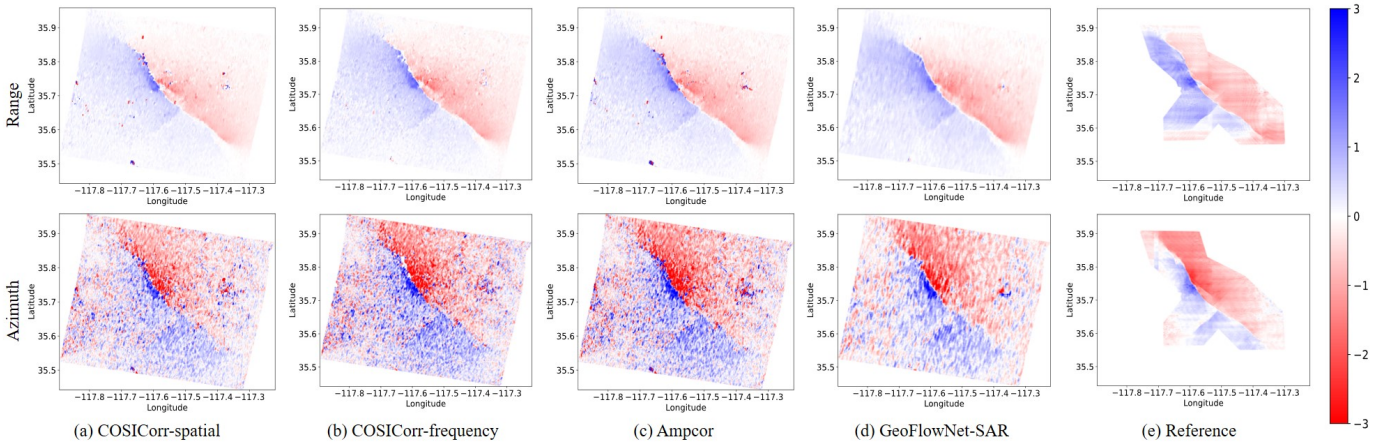

Fig. 9. Displacement maps generated by the four models—COSICorr-spatial, COSICorr-frequency, Ampcor, and GeoFlowNet-SAR on Ridgecrest Earthquake images. The first column shows displacement maps in the range direction, and the second in the azimuth direction. The results are presented in displacement distance (meters). The reference was computed using satellite optical imagery.

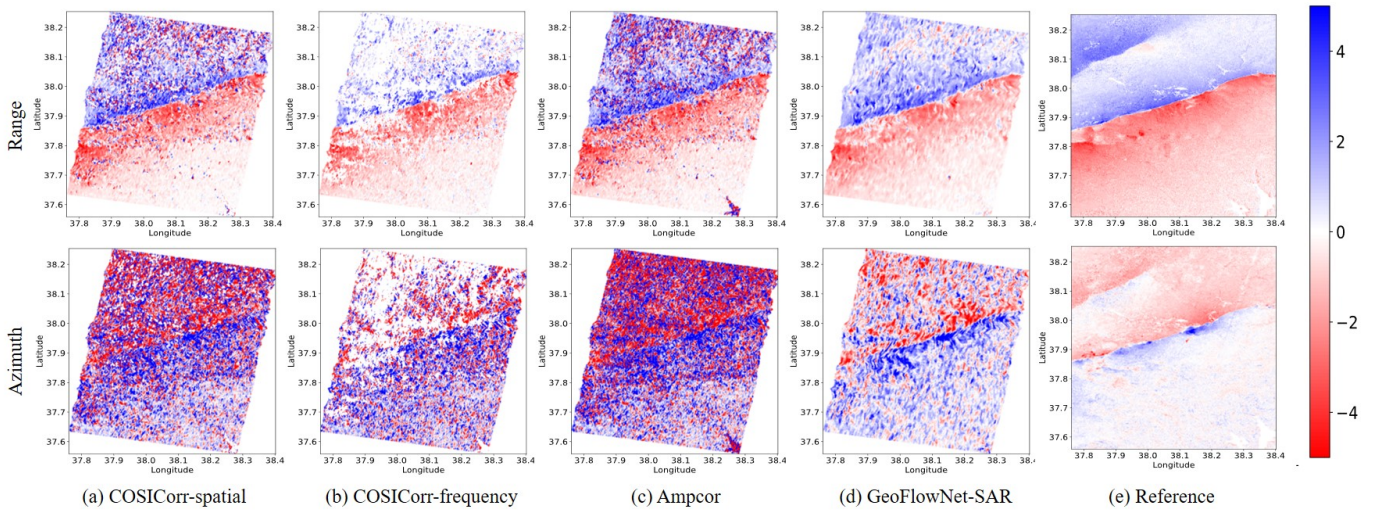

Fig. 10. Displacement maps generated by the four models—COSICorr-spatial, COSICorr-frequency, Ampcor, and GeoFlowNet-SAR on Turkey–Syria Earthquake images. The first column shows displacement maps in the range direction, and the second in the azimuth direction. The results are presented in displacement distance (meters). The reference was computed using satellite optical imagery.

processing [41]. Optical image correlation methods are known to be more robust against high-frequency noise (e.g., speckle), as optical image does not have the coherent scattering effects of SAR. Moreover, there were no cloud artifacts during the acquisition, and the optical resolution was superior, especially in azimuth. As such, the optical results serve as independent reference baselines (even if not a perfect ground truth), not affected by the model under evaluation.

COSICorr-spatial, COSICorr-frequency, and Ampcor were configured using the optimal parameter settings validated on the synthetic dataset, while GeoFlowNet-SAR employed the model previously trained on the synthetic data. The displacement maps generated by the four methods are shown in Fig.9. The pre-image, acquired on June 22, 2019, and the post-image, acquired on July 16, 2019, are shown in Fig.7.

Both COSICorr-spatial and COSICorr-frequency capture some displacement information in the overall image structure, but exhibit noticeable noise and lack fine details, especially in boundary and small-area displacement estimations. The Ampcor method demonstrates better detail capture, particularly along edges, but still suffers from significant noise artifacts, especially around the earthquake zone, making it challenging to accurately interpret the ground displacement. GeoFlowNet-SAR shows advantages in capturing primary displacement patterns and details, particularly in the earthquake region and complex boundary areas. It provides sharper details and reduced noise levels compared to the other methods. However, its superiority is not uniform across the entire map. In regions with lower signal-to-noise ratios or subtle displacement variations, the improvements are less pronounced. Additionally, while GeoFlowNet-SAR demonstrates better performance near fault ruptures, it is still susceptible to residual artifacts in these highly complex regions. In the vicinity of fault ruptures, where sharp discontinuities dominate displacements, the three comparison methods struggle to provide realistic displacement estimations, often resulting in outliers near the rupture zones. GeoFlowNet-SAR reduces such biases and better captures near-field displacement patterns in this real-world case.

2) Turkey–Syria earthquake: As second test case, the Turkey–Syria earthquakes occurred on February 6, 2023, in

Southern Turkey near the Syrian border. Three seismic events were recorded on that day, with the USGS identifying the events as a shallow strike-slip fault earthquakes. Based on the focal mechanism of the main earthquake, coupled with aftershocks, and initial optically-derived image correlation results [44], this earthquake sequence initiated on the northeast-southwest left-lateral Narlı fault, before triggering much larger slip on the northeast-southwest left-lateral East Anatolian Fault (EAF), before being followed several hours later by left-lateral slip on the east-west Çardak fault.

Similar to the previous case study, this section compares the proposed model with COSICorr-spatial, COSICorr-frequency, and Ampcor using SAR images spanning the earthquake event. As with the previous example, there is a lack of publicly available ground truth displacement statistics for this event. Therefore, the comparison is conducted through visual inspection of the displacement maps generated by each method, highlighting their differences and similarities, and showcasing the performance of the different approaches in this particular case. Similar to the Ridgecrest earthquake, we introduce the prediction results of ground displacement estimation using optical imagery for this earthquake case as a reference for comparison. The optical reference results in this case were generated from Sentinel-2 images using the COSI-Corr-frequency method, following the same procedure as in the Ridgecrest case. These reference maps were also independently cleaned and validated by experts, ensuring their use as unbiased benchmarks [44]. The displacement maps generated by the four methods are shown in Fig.10. The pre-image, acquired on January 29, 2023, and the post-image, acquired on February 10, 2023, are shown in Fig.8.

In this earthquake event, COSICorr-spatial and COSICorr-frequency capture the general outline of the displacement pattern but struggle with finer details. Particularly in boundary areas and noise suppression, they exhibit noticeable texture noise, making it challenging to delineate the actual fault structure. The Ampcor method demonstrates some improvement in capturing edge details within the earthquake zone, but substantial noise persists, especially in regions with smaller displacements, leading to instability and reduced reliability in these areas. GeoFlowNet-SAR shows noticeable advantages in the near-field region of the actual fault rupture. It achieves better consistency on both sides of the fault, effectively suppresses noise artifacts, and provides clearer displacement patterns in complex areas. Furthermore, it recovers the more subtle displacements associated with the eastern termination of the Çardak fault (north of the EAF). These results indicate that GeoFlowNet-SAR is well-suited for displacement field estimation in real earthquake events, leveraging SAR imagery for all-weather, round-the-clock observation and enabling a timely response to seismic events. However, while GeoFlowNet-SAR demonstrates superior performance in regions with significant displacement, its advantages are less pronounced in areas with low signal-to-noise ratios or subtle displacement variations, where residual artifacts remain visible. Additionally, the method's performance can be sensitive to variations in data quality and resolution, which may affect its robustness in highly heterogeneous regions. These limitations suggest room for further improvement to enhance its generalization and adaptability across diverse scenarios.

Although displacement estimation results from optical images are introduced for visual comparison, these results cannot be treated as strict ground truth. This is due to fundamental differences in the acquisition geometries between SAR and optical sensors, particularly along the range direction for SAR, which cannot be directly compared with east-west displacements in optical imagery without assuming a vertical component. Furthermore, only partial spatial overlap exists between the SAR and optical images, and the azimuth component, which is more comparable to optical north-south motion, is the noisiest in the Sentinel-1 data. Therefore, mean absolute error (MAE) statistics between SAR-derived and optical-derived displacements are not reported, as they would not reflect the deviation from ground truth, but only the differences between two modalities under distinct observation constraints.

D. Runtime Comparison Analysis

To evaluate the computational efficiency of the proposed GeoFlowNet-SAR method in the task of ground displacement estimation, we conducted a series of comparative experiments using both synthetic and real earthquake data (see Tab. II). The synthetic dataset serves as a controlled environment to assess the fundamental performance of the algorithms, while the real dataset evaluates their practical applicability. The comparison involves three methods, COSICorr-spatial, COSICorr-frequency and Ampcor, all executed on a 16-core CPU, while the proposed GeoFlowNet-SAR runs on a GPU.GeoFlowNet-optical is not included in the runtime analysis, as its results were generated on a different hardware setup, making direct comparison inappropriate. Given its architecture is nearly identical to GeoFlowNet-SAR, their runtimes are theoretically expected to be almost the same.

TABLE II
RUNTIME (SECONDS) COMPARISON ON ONE SYNTHETIC SAMPLE (1024×1024) AND THE TURKEY-SYRIA EARTHQUAKE (9514×24418)

Methods \ Datasets	image 1024×1024	The Turkey–Syria Earthquake
GeoFlowNet-SAR	**3.11s**	**108.94s**
COSICorr-spatial	6.14s	1286.58s
COSICorr-frequency	5.18s	162.92s
Ampcor	53.91s	12559.96s

1) Synthetic Earthquake Database: The first experiment was conducted on a synthetically generated dataset with a resolution of 1024×1024, which provides a standardized baseline for performance comparison across different methods. The experimental results demonstrate that GeoFlowNet-SAR achieves a runtime of only 3.11 seconds, significantly outperforming COSICorr-spatial (6.14s), COSICorr-frequency (5.18s), and Ampcor (53.91s).

2) Real Earthquake Case: The second experiment was conducted on real earthquake data acquired from the Turkey–Syria earthquake event, with an image resolution

of 9514×24418. This dataset was selected as a representative case for performance evaluation. The experimental results reveal that GeoFlowNet-SAR completes the task in 108.94 seconds, significantly outperforming COSICorr-spatial (1286.58s), COSICorr-frequency (162.92s), and Ampcor (12559.96s). Specifically, GeoFlowNet-SAR achieves an 11.81-fold speedup compared to COSICorr-spatial, a 1.50-fold improvement over COSICorr-frequency, and a 115-fold acceleration relative to Ampcor.

These results underscore the advantages of leveraging GPU-based deep learning architectures for ground displacement estimation. By adopting an optimized network structure and parallel computation capabilities, GeoFlowNet-SAR significantly reduces computational time while maintaining high estimation accuracy, demonstrating its potential for large-scale applications. Moreover,GeoFlowNet-SAR is scalable when processing large-scale real-world earthquake datasets.

V. Conclusion

This paper proposes a comprehensive UNet-based deep learning framework, GeoFlowNet-SAR, which is designed to estimate ground displacement from SAR image pairs with sub-pixel precision. Compared to previous methods, GeoFlowNet-SAR performs dense sub-pixel displacement estimation, reducing the impact of spatial detail smoothing caused by noise removal in earlier approaches. It also has superior performance in regions with abrupt displacement changes or discontinuities, outperforming state-of-the-art methods in near-field displacement estimation for earthquakes. A high-quality synthetic dataset generated based on realistic fault slip models was utilized to train the model and evaluate its performance using quantitative metrics, demonstrating the improvements of GeoFlowNet-SAR compared to other methods. Additionally, to validate the robustness and transferability of the model, estimations were made and analyzed for two real earthquake cases. The ability of GeoFlowNet-SAR to provide high-resolution displacement estimates near fault boundaries holds particular geophysical significance. Such detailed observations enable better characterization of near-field deformation, which is essential for constraining earthquake source parameters, including fault geometry, rupture extent, and slip distribution. Accurate mapping of these features supports improved understanding of fault mechanics and contributes to refining seismic hazard assessments. In future work, we will focus on integrating multi-source remote sensing data to estimate surface displacements. By leveraging the complementary information from different sources, the estimation errors inherent in single-source data could be corrected.

References

[1] S. Leprince, S. Barbot, F. Ayoub, and J.-P. Avouac, "Automatic and precise orthorectification, coregistration, and subpixel correlation of satellite images, application to ground deformation measurements," *IEEE Transactions on Geoscience and Remote Sensing*, vol. 45, no. 6, pp. 1529–1558, 2007.

[2] T. Heid and A. Kääb, "Evaluation of existing image matching methods for deriving glacier surface displacements globally from optical satellite imagery," *Remote Sensing of Environment*, vol. 118, pp. 339–355, 2012.

[3] J. Hollingsworth, S. Leprince, F. Ayoub, and J.-P. Avouac, "Deformation during the 1975–1984 krafla rifting crisis, ne iceland, measured from historical optical imagery," *Journal of Geophysical Research: Solid Earth*, vol. 117, no. B11, 2012.

[4] P. Lacroix, G. Araujo, J. Hollingsworth, and E. Taipe, "Self-entrainment motion of a slow-moving landslide inferred from landsat-8 time series," *Journal of Geophysical Research: Earth Surface*, vol. 124, no. 5, pp. 1201–1216, 2019.

[5] J. F. Dolan and B. D. Haravitch, "How well do surface slip measurements track slip at depth in large strike-slip earthquakes? the importance of fault structural maturity in controlling on-fault slip versus off-fault surface deformation," *Earth and Planetary Science Letters*, vol. 388, pp. 38–47, 2014.

[6] C. Milliner, J. Dolan, J. Hollingsworth, S. Leprince, and F. Ayoub, "Comparison of coseismic near-field and off-fault surface deformation patterns of the 1992 mw 7.3 landers and 1999 mw 7.1 hector mine earthquakes: Implications for controls on the distribution of surface strain," *Geophysical Research Letters*, vol. 43, no. 19, pp. 10–115, 2016.

[7] G. Cheng and W. D. Barnhart, "Permanent co-seismic deformation of the 2013 mw7. 7 baluchistan, pakistan earthquake from high-resolution surface strain analysis," *Journal of Geophysical Research: Solid Earth*, vol. 126, no. 3, p. e2020JB020622, 2021.

[8] R. Zinke, J. Hollingsworth, J. F. Dolan, and R. Van Dissen, "Three-dimensional surface deformation in the 2016 mw 7.8 kaikōura, new zealand, earthquake from optical image correlation: Implications for strain localization and long-term evolution of the pacific-australian plate boundary," *Geochemistry, Geophysics, Geosystems*, vol. 20, no. 3, pp. 1609–1628, 2019.

[9] W. D. Barnhart, R. D. Gold, and J. Hollingsworth, "Localized fault-zone dilatancy and surface inelasticity of the 2019 ridgecrest earthquakes," *Nature Geoscience*, vol. 13, no. 10, pp. 699–704, 2020.

[10] N. Ajorlou, J. Hollingsworth, Z. Mousavi, A. Ghods, and Z. Masoumi, "Characterizing near-field surface deformation in the 1990 rudbar earthquake (iran) using optical image correlation," *Geochemistry, Geophysics, Geosystems*, vol. 22, no. 6, p. e2021GC009704, 2021.

[11] C. Zach, T. Pock, and H. Bischof, "A duality based approach for realtime tv-l 1 optical flow," in *Pattern Recognition: 29th DAGM Symposium, Heidelberg, Germany, September 12-14, 2007. Proceedings 29*. Springer, 2007, pp. 214–223.

[12] H. Hirschmuller, "Stereo processing by semiglobal matching and mutual information," *IEEE Transactions on pattern analysis and machine intelligence*, vol. 30, no. 2, pp. 328–341, 2007.

[13] M. Guizar-Sicairos, S. T. Thurman, and J. R. Fienup, "Efficient subpixel image registration algorithms," *Optics letters*, vol. 33, no. 2, pp. 156–158, 2008.

[14] A. V. Nefian, K. Husmann, M. Broxton, V. To, M. Lundy, and M. D. Hancher, "A bayesian formulation for sub-pixel refinement in stereo orbital imagery," in *2009 16th IEEE international conference on image processing (ICIP)*. IEEE, 2009, pp. 2361–2364.

[15] R. Michel and J.-P. Avouac, "Deformation due to the 17 august 1999 izmit, turkey, earthquake measured from spot images," *Journal of Geophysical Research: Solid Earth*, vol. 107, no. B4, pp. ETG–2, 2002.

[16] C. W. Milliner, J. F. Dolan, J. Hollingsworth, S. Leprince, F. Ayoub, and C. G. Sammis, "Quantifying near-field and off-fault deformation patterns of the 1992 mw 7.3 landers earthquake," *Geochemistry, Geophysics, Geosystems*, vol. 16, no. 5, pp. 1577–1598, 2015.

[17] C. P. Scott, J. R. Arrowsmith, E. Nissen, L. Lajoie, T. Maruyama, and T. Chiba, "The m7 2016 kumamoto, japan, earthquake: 3-d deformation along the fault and within the damage zone constrained from differential lidar topography," *Journal of Geophysical Research: Solid Earth*, vol. 123, no. 7, pp. 6138–6155, 2018.

[18] S. L. Antoine, Y. Klinger, A. Delorme, K. Wang, R. Bürgmann, and R. D. Gold, "Diffuse deformation and surface faulting distribution from submetric image correlation along the 2019 ridgecrest, california, ruptures," *Bulletin of the Seismological Society of America*, vol. 111, no. 5, pp. 2275–2302, 2021.

[19] P. A. Rosen, S. Hensley, G. Peltzer, and M. Simons, "Updated repeat orbit interferometry package released," *Eos, Transactions American Geophysical Union*, vol. 85, no. 5, pp. 47–47, 2004.

[20] A.-M. Rosu, M. Pierrot-Deseilligny, A. Delorme, R. Binet, and Y. Klinger, "Measurement of ground displacement from optical satellite image correlation using the free open-source software micmac," *ISPRS Journal of Photogrammetry and Remote Sensing*, vol. 100, pp. 48–59, 2015.

[21] E. Rupnik, M. Daakir, and M. Pierrot Deseilligny, "Micmac–a free, open-source solution for photogrammetry," *Open geospatial data, software and standards*, vol. 2, pp. 1–9, 2017.

[22] C. Milliner and A. Donnellan, "Using daily observations from planet labs satellite imagery to separate the surface deformation between the 4 july m w 6.4 foreshock and 5 july m w 7.1 mainshock during the 2019 ridgecrest earthquake sequence," *Seismological Research Letters*, vol. 91, no. 4, pp. 1986–1997, 2020.

[23] N. Van Puymbroeck, R. Michel, R. Binet, J.-P. Avouac, and J. Taboury, "Measuring earthquakes from optical satellite images," *Applied Optics*, vol. 39, no. 20, pp. 3486–3494, 2000.

[24] X. Tong, Z. Ye, Y. Xu, S. Liu, L. Li, H. Xie, and T. Li, "A novel subpixel phase correlation method using singular value decomposition and unified random sample consensus," *IEEE Transactions on Geoscience and Remote Sensing*, vol. 53, no. 8, pp. 4143–4156, 2015.

[25] T. A. Scambos, M. J. Dutkiewicz, J. C. Wilson, and R. A. Bindschadler, "Application of image cross-correlation to the measurement of glacier velocity using satellite image data," *Remote sensing of environment*, vol. 42, no. 3, pp. 177–186, 1992.

[26] X. Tong, Z. Ye, Y. Xu, S. Gao, H. Xie, Q. Du, S. Liu, X. Xu, S. Liu, K. Luan, *et al.*, "Image registration with fourier-based image correlation: A comprehensive review of developments and applications," *IEEE Journal of Selected Topics in Applied Earth Observations and Remote Sensing*, vol. 12, no. 10, pp. 4062–4081, 2019.

[27] G. Facciolo, C. De Franchis, and E. Meinhardt, "Mgm: A significantly more global matching for stereovision," in *BMVC 2015*, 2015.

[28] S. Li, S. Leinss, and I. Hajnsek, "Cross-correlation stacking for robust offset tracking using sar image time-series," *IEEE Journal of Selected Topics in Applied Earth Observations and Remote Sensing*, vol. 14, pp. 4765–4778, 2021.

[29] E. Pathier, E. Fielding, T. Wright, R. Walker, B. Parsons, and S. Hensley, "Displacement field and slip distribution of the 2005 kashmir earthquake from sar imagery," *Geophysical research letters*, vol. 33, no. 20, 2006.

[30] Y. LeCun, B. Boser, J. S. Denker, D. Henderson, R. E. Howard, W. Hubbard, and L. D. Jackel, "Backpropagation applied to handwritten zip code recognition," *Neural computation*, vol. 1, no. 4, pp. 541–551, 1989.

[31] A. Krizhevsky, I. Sutskever, and G. E. Hinton, "Imagenet classification with deep convolutional neural networks," *Advances in neural information processing systems*, vol. 25, 2012.

[32] J. Wang, M. Zhang, W. Li, and R. Tao, "A multistage information complementary fusion network based on flexible-mixup for hsi-x image classification," *IEEE Transactions on Neural Networks and Learning Systems*, 2023.

[33] B. Zhao, M. Zhang, W. Li, X. Song, Y. Gao, Y. Zhang, and J. Wang, "Intermediate domain prototype contrastive adaptation for spartina alterniflora segmentation using multi-temporal remote sensing images," *IEEE Transactions on Geoscience and Remote Sensing*, 2024.

[34] Y. Weng, S.-T. Quek, and J. K.-W. Yeoh, "Robust vision-based sub-pixel level displacement measurement using a complementary strategy," *Mechanical Systems and Signal Processing*, vol. 223, p. 111898, 2025.

[35] R. Yang and P. Guo, "Of-net: Deep-learning based sub-pixel optical flow estimation with multi-scale convolutional neural network," in *International Manufacturing Science and Engineering Conference*, vol. 84263. American Society of Mechanical Engineers, 2020, p. V002T08A022.

[36] T. Montagnon, S. Giffard-Roisin, M. Dalla Mura, M. Marchandon, E. Pathier, and J. Hollingsworth, "Sub-pixel displacement estimation with deep learning: Application to optical satellite images containing sharp displacements," *Journal of Geophysical Research: Machine Learning and Computation*, vol. 1, no. 4, p. e2024JH000174, 2024.

[37] T. Montagnon, J. Hollingsworth, E. Pathier, M. Marchandon, M. Dalla Mura, and S. Giffard-Roisin, "Geoflownet: Fast and accurate sub-pixel displacement estimation from optical satellite images based on deep learning." *arXiv preprint*, 2024.

[38] L. Guerriero, D. Di Martire, D. Calcaterra, and M. Francioni, "Digital image correlation of google earth images for earth's surface displacement estimation," *Remote sensing*, vol. 12, no. 21, p. 3518, 2020.

[39] A. Dosovitskiy, P. Fischer, E. Ilg, P. Hausser, C. Hazirbas, V. Golkov, P. Van Der Smagt, D. Cremers, and T. Brox, "Flownet: Learning optical flow with convolutional networks," in *Proceedings of the IEEE international conference on computer vision*, 2015, pp. 2758–2766.

[40] E. Ilg, N. Mayer, T. Saikia, M. Keuper, A. Dosovitskiy, and T. Brox, "Flownet 2.0: Evolution of optical flow estimation with deep networks," in *Proceedings of the IEEE conference on computer vision and pattern recognition*, 2017, pp. 2462–2470.

[41] S. Aati, C. Milliner, and J.-P. Avouac, "A new approach for 2-d and 3-d precise measurements of ground deformation from optimized registration and correlation of optical images and ica-based filtering of image geometry artifacts," *Remote Sensing of Environment*, vol. 277, p. 113038, 2022.

[42] P. A. Rosen, E. M. Gurrola, P. Agram, J. Cohen, M. Lavalle, B. V. Riel, H. Fattahi, M. A. Aivazis, M. Simons, and S. M. Buckley, "The insar scientific computing environment 3.0: A flexible framework for nisar operational and user-led science processing," in *IGARSS 2018 - 2018 IEEE International Geoscience and Remote Sensing Symposium*, 2018, pp. 4897–4900.

[43] T. Montagnon, S. Giffard-Roisin, M. Dalla Mura, M. Marchandon, E. Pathier, and J. Hollingsworth, "Sub-Pixel Displacement Estimation with Deep Learning: Application to Optical Satellite Images Containing Sharp Displacements," Oct. 2023, working paper or preprint. [Online]. Available: https://hal.science/hal-04256681

[44] H. Karabulut, S. E. Güvercin, J. Hollingsworth, and A. Ö. Konca, "Long silence on the east anatolian fault zone (southern turkey) ends with devastating double earthquakes (6 february 2023) over a seismic gap: implications for the seismic potential in the eastern mediterranean region," *Journal of the Geological Society*, vol. 180, no. 3, pp. jgs2023–021, 2023.